Journal of Materials & Manufacturing Technology

www.jmmt.reapress.com

J. Mater. Manuf. Technol. Vol. 3, No. 1 (2026) 31-55.

Paper Type: Original Article

Nanocomposite Coatings for Subsea Pipeline Corrosion Protection in Nigeria: Harnessing the Functionalities of Locally Sourced Bentonite and Rubber

Patrick P Obot[1,*], Aondona Paul Ihom[1], Aniekan Offiong[1], Idorenyin E Markson[1]

[1] Department of Mechanical and Aerospace Engineering University of Uyo, PMB 1017, Uyo, Akwa Ibom State, Nigeria; obotuv@yahoo.com; obotman@gmail.com; ihomaondona@uniuyo.edu.ng; offionga1234@gmail.com; idorenyin1234@gmail.com.

Citation:

Received: ----- *Revised:* ----- *Accepted:*---	Obot, P. P., Ihom, A. P., Offiong, A., & Markson, I. E. (2026). Nanocomposite coatings for subsea pipeline corrosion protection in Nigeria: Harnessing the functionalities of locally sourced bentonite and rubber. *Journal of Materials & Manufacturing Technology*, *3*(1), 31-55.

Abstract

The study synthesized and characterized a polymer-rubber-organoclay nanocomposite coating for corrosion protection of X52-linepipe steel in a marine environment. A Blend of Diglycidyl Ether Bisphenol A (DGEBA) and Epoxidized Hydroxyl-Terminated Polybutadiene (EHTPB) rubber, with its nanocomposite coatings, was synthesized by solution exfoliation/intercalation. The degree of Epoxy Polymer (EP)-EHTPB modification and fracture toughness was evaluated by Fourier Transform Infrared Spectroscopy (FTIR) and Scanning Electron Microscope (SEM), while the degree of intercalation/exfoliation of nanoparticles was determined using X-Ray Diffractometer (XRD) and SEM. The mechanical, adhesion, and barrier properties of the coatings were determined according to American Society for Testing and Materials (ASTM) standards, while their corrosion behaviour was evaluated using total immersion and Electrochemical Impedance Spectroscopy (EIS) techniques. The mechanical, adhesion, and barrier properties of the modified EP-10R and EP-10R-omNa-MMt nanocomposite coatings were enhanced compared to those of the EP. The protective properties of the nanocomposite coatings were higher compared to those of the EP, with EP-10R-3wt.%omNa-MMt showing the highest protection efficiency. The study concludes that by effectively integrating locally sourced bentonite as advanced nanomaterials, the synthesized polymer-rubber-organoclay nanocomposite coating shows the potential to significantly enhance the corrosion resistance of subsea pipelines.

Keywords: Bentonite, Nanocomposite, Coating, Corrosion, Subsea, Pipeline.

1 | Introduction

Subsea pipelines are essential to the global energy supply chain, enabling efficient transportation of hydrocarbons across various oilfield environments. These pipelines, with diameters ranging from small (0.5 inches) to large (48 inches), are manufactured for durability, high strength, and safety in challenging marine

Corresponding Author: obotman@gmail.com

https://doi.org/10.48314/jmmt.vi.35

Licensee System Analytics. This article is an open access article distributed under the terms and conditions of the Creative Commons Attribution (CC BY) license (http://creativecommons.org/licenses/by/4.0).

environments [1], [2]. However, the marine environment exposes these assets to aggressive corrosive species, which compromise structural integrity and lead to costly repairs or environmental hazards if not effectively managed [3], [4]. Traditional approaches, such as polymer-based coatings, provide promising protection by forming a barrier against corrosive agents. Nonetheless, limitations in performance longevity, especially under severe subsea conditions, necessitate the exploration of advanced coating materials with enhanced durability [5], [6]. Polymer coatings, such as epoxy and polyurethane, have become standard solutions in the Nigerian oil and gas industry due to their low cost, ease of application, and protective performance; however, these materials often fail to consistently meet long-term demands in subsea applications due to cracking, delamination, and permeability under harsh conditions [7], [8]. Corrosion in subsea environments is accelerated by a combination of seawater salinity, temperature variations, and mechanical stresses [9], [10]. Conventional organic coatings have been widely adopted due to their cost-effectiveness and mechanical properties. However, these coatings often degrade over time, becoming susceptible to cracking and delamination, especially under prolonged exposure to extreme conditions such as Ultraviolet (UV) light, high pressure, and microbial activity [8], [6]. Commonly used pipeline coatings, including Fusion-Bonded Epoxy (FBE) and multi-layer Polypropylene (PP) systems, while effective in many applications, may not fully meet the demands of harsh subsea environments due to their brittle nature and susceptibility to physical damage, leading to ongoing research on novel coating formulations [7], [11].

Recent advancements in nanotechnology have opened avenues for developing high-performance coatings. Specifically, polymer nanocomposites reinforced with nanoscale fillers have demonstrated improved mechanical, thermal, and barrier properties. Montmorillonite (MMt), a smectite clay mineral commonly obtained from bentonite, has emerged as a highly effective nano-filler due to its high surface area, aspect ratio, and ion-exchange capacity [12], [13]. When dispersed within a polymer, MMt nanoparticles create a tortuous path that enhances the resistance of the coating to permeation by corrosive agents, which is crucial for subsea applications [12], [14]. However, achieving this performance improvement while maintaining the coating's flexibility and mechanical integrity remains a significant challenge. However, achieving this performance improvement while maintaining the flexibility and mechanical integrity of the coating remains a significant challenge [15], [16]. This study addresses the need for sustainable, high-performance coatings by exploring the use of locally sourced Nigerian bentonite in nanocomposite formulations. Although Nigeria possesses abundant bentonite resources across various states [17], [18] these deposits are often of low-grade calcium bentonite, necessitating beneficiation to improve their quality for industrial applications [19]. There has been limited development of these resources into high-performance coatings suited for offshore applications. As a result, the oil and gas industry remains heavily dependent on imported materials with high costs and limiting local innovation [17], [19]. By utilizing indigenous resources, this work aims to produce a cost-effective and durable nanocomposite coating that addresses the specific corrosion challenges posed by Nigeria's marine environment. Through effective synthesis and characterization, the study seeks to establish a foundation for locally driven innovation in protective coatings, ultimately reducing dependency on foreign imports and contributing to the sustainable development of Nigeria's energy infrastructure.

2|Materials and Methods

2.1|Materials and Chemicals

The Diglycidyl Ether Bisphenol A (DGEBA) liquid epoxy resin with properties as given in *Table 1*. Epoxidized Hydroxy-Terminated Polybutadiene (EHTPB) rubber (*Table 2).* Polyamine (A60) having an amine value of 460 mg KOH/g, Toluene Diisocyanate (TDI), Ethyl acetate, Dibutyltin Dilaurate (DBTDL), and Dioctyl Sebacate (DOS) were purchased from Mike-Ene Equipment Co., Uyo. The materials were used as received without any further treatment. The bentonite was locally sourced from the southeast region of Nigeria *Table 3*. The 2-inch (ID) API 5L X-52 grade of steel in the form of linepipe with chemical compositions as given in *Table 4*. was obtained from Harmony Steel and Construction Co. Ltd., Port Harcourt. The linepipe stock material is available in the thickness of schedule 80 (8.56mm), and 40 feet (12,192mm) long. Other materials include sodium hexametaphosphate, sodium fluoride, silver nitrate solution, Octadecyl dimethyl phenmethyl

ammonium chloride, Isopropyl Alcohol (IPA), and distilled water. Weighing balance, thermostatically controlled oven, mechanical sieves, centrifuge, Teflon stirrer, X-Ray Diffractometer (XRD), Scanning Electron Microscope (SEM), Energy Dispersive X-ray (EDX), Fourier Transform Infrared Spectroscopy (FTIR) spectrometer, mould, impact tester, universal tensile machine, thickness-measuring gage, test chamber, magnifier, cutting tool, semitransparent pressure-sensitive tape, impedance spectrum analyzer, granite rod, silver-silver-chloride, and PC terminal, three-neck flask, desiccator, planetary ball mill, Sonic dismembrator, beakers, filter paper, vacuum filter, ImageJ, and ORIGINPRO software.

Table 1. Properties of DGEBA liquid epoxy resin.

Properties	Values
Molecular formula	$C_{21}H_{24}O_4$ or $C_2H_3OCH_2OC_6H_3C_3H_6C_6H_5OCH_2C_2H_3O$
Density	1.17 g/cm^3 at 25 °C
Molecular weight	340.41
Melting point	40-44 °C
Water solubility	Insoluble
Form	Viscous liquid
Colour	White
Solubility	DMSO (up to 30 mg/ml) or Ethanol (up to 15 mg/ml)
Refractive index	1.5735
Storage temperature	Inert atmosphere, 2-8°C

Table 2. Properties of EHTPB rubber modifier.

Properties	Values
Density	0.913 g/mL at 25 °C
Hydroxyl content	1.06 mmol/g
Epoxy content	3.26 mmol/g
Moisture content	0.015%
Mn content	3000 g/mol
Molecular weight	3280

Table 3. Locations of locally sourced clay minerals for characterization.

Clay Sample	Symbol	State	L.G.A	Location
Achalla-Agu	Ach	Anambra	Oyi	6.14°N/ 6.45°E

Table 4. Chemical composition of API 5L X52 steel substrate

Elements	Weight Percent (%) Max.
C	0.15562
Si	0.22471
Mn	0.96740
P	0.02571
Cr	0.03676
Mo	0.04706
Ti	0.03067
Al	0.01233
Co	0.03567
V	0.03982
Fe	98.42425

2.2 | Geology of Bentonite Location

The Achalla-Agu bentonite clay deposit is located within the geological setting of Anambra State, southeastern Nigeria, an area renowned for its rich mineral endowment and diverse geological formations. Specifically, the clay deposit is situated within the Awka North Local Government Area, close to the town of Achalla-Agu. This geographical region is characterized by its complex geological history, shaped by sedimentary processes, tectonic activity, and weathering phenomena over millions of years. The geological formation hosting the Achalla-Agu bentonite clay is primarily composed of sedimentary rocks, including shale, sandstone, and claystone, which have undergone extensive weathering and alteration processes.

The clay deposit itself is believed to have originated from the alteration of volcanic ash deposits, with the subsequent enrichment of bentonite minerals due to hydrothermal and diagenetic processes. The topography of the Achalla-Agu area is characterized by rolling hills, shallow valleys, and dissected plateaus, indicative of its position within the Nigerian Basement Complex. This geological setting has played a pivotal role in the formation and preservation of the bentonite clay deposit, with factors such as drainage patterns, soil erosion, and vegetation cover influencing its distribution and characteristics.

2.3 | Methods

The Achalla-Agu bentonite (Ca-bentonite) used in the study was beneficiated and modified to synthesize the nanoparticles. The clay is composed of approximately 79 wt.% of the 2:1 group of phyllosilicate minerals with MMt accounting for about 45 % of the total mass. The bentonite has a clay fraction of about 70.92 % and lower silt and sand fractions of 1.74 and 27.34% respectively.

Due to its crystalised structure and mineralogical composition, the Achalla-Agu bentonite has higher CEC (53 $cmol^+/kg$), specific surface area (559 m^2/g), swell index (15.2 mL/2 g), and shrinkage limit (41.9%). The specific gravity and hydraulic conductivity were found to be 2.75 and 7.1 x 10^{-11} m/s respectively.

2.3.1 | Synthesis of polymer nanocomposite coatings

The matrix material used in synthesizing the EP-R-omNa-MMt nanocomposite coating is the DGEBA liquid epoxy resin. In considering the inherent brittleness of the epoxy resin, EHTPB rubber was selected as the toughening modifier. Polyamine (A60) having an amine value of 460 mg KOH/g was used as a curing agent and TDI as an intercalation solution.

Ethyl acetate was used to dissolve the monomers and DBTDL and DOS were used as catalysts. As represented in *Table 6*. the polymer nanocomposite coating was synthesized by solution intercalation of varying amounts of the organically modified Na-MMt and EHTPB rubber. The solution mixing technique was used to synthesize the polymer-organoclay nanocomposite coatings.

A maximum content of 7 wt. % omNa-MMt nanoparticle was selected for dispersion to achieve an intercalated/exfoliated nanostructure that can be detected by XRD analysis. According to Morgan and Gilman [20], an exfoliated clay spacing in the polymer matrix cannot be observed at $2\theta < 1°$ with XRD analysis. For this reason, Bragg's law was used to determine the basal spacing (d) at $2\theta = 1°$ required for detection of an exfoliated nanostructure using XRD analysis *Eq. (1)*.

From the XRD interlayer analysis, it was observed that the d-spacing of the synthesized omNa-MMt nanoparticles (3.62 nm) was less than the calculated d-spacing value of 8.8 nm. This makes it detectable by XRD analysis and suitable for the synthesis of polymer-organoclay nanocomposite coating.

Table 5. Compositions of synthesized polymer nanocomposite coatings.

Sample	Weight Percent (wt. %)		
	DGEBA	**EHTPB**	**omNa-MMT**
Reference coupons			
Achalla-Agu omNa-MMt clay	-	-	100
Cured Epoxy Polymer (EP)	100	-	-
Modified-Epoxy Polymer			
EP-5R-0omNa^+-MMt	95	5	-
EP-10R-0omNa^+-MMt	90	10	-
EP-15R-0omNa^+-MMt	85	15	-
EP-25R-0omNa^+-MMt	75	25	-
Epoxy-R-omNa-MMt nanocomposite coating			
EP-R-1omNa^+-MMt	89	10	1
EP-R-3omNa^+-MMt	87	10	3
EP-R-5omNa^+-MMt	85	10	5
EP-R-7omNa^+-MMt	83	10	7

$$d = \frac{n\lambda}{2\sin\theta}, \quad (1)$$

where d is the required basal spacing of the nanoparticles, λ is the wavelength of the X-rays (0.154 nm), θ is the scanned angle of the nanoparticles (0.5°), and n is the order of diffraction (n = 1).

To determine the expanded volume of nanoparticles in polymer matrix, assuming an ideal packing of the omNa-MMt nanoparticles in the matrix of the polymer will expand the interlayer spacing of the particles by X nm, the width by W, and the length by L, the volume fraction of the expanded omNa-MMt nanoparticles was calculated as follows:

$$V_{omNa-MMT} = 1 \text{ x } L \text{ x } W, \quad (2)$$
$$V_{pm} = X \text{ x } L \text{ x } W, \quad (3)$$
$$V_{total} = (1 + X) \text{ x } L \text{ x } W, \quad (4)$$
$$V_{f_{omNa-MMT}} = \frac{1 \text{ x } L \text{ x } W}{(1 + X) \text{ x } L \text{ x } W}, \quad (5)$$
$$V_{f_{omNa-MMT}} = \frac{1}{(1 + X)}, \quad (6)$$

where $V_{omNa-MMT}$ is the volume of the organically modified Na- MMt nanoparticles for one plane, V_{pm} is the volume of the polymer matrix packed with omNa-MMT nanoparticles, V_{total} is the total volume of nanoparticles for one plane and polymer matrix packed with omNa-MMT nanoparticles, and $V_{f_{omNa-MMT}}$ is the volume fraction of the organically modified Na- MMt nanoparticles.

At 7 wt. % loading of omNa-MMt nanoparticles into the matrix of the polymer, the volume fraction of the omNa-MMt was calculated as follows:

$$V_{f_{omNa-MMT}} = \frac{V_{omNa-MMT}}{V_{pm} + V_{omNa-MMT}}, \quad (7)$$
$$V_{omNa-MMT} = \frac{m_{omNa-MMT}}{D_{omNa-MMT}}, \quad (8)$$
$$V_{pm} = \frac{m_{pm}}{D_{pm}}, \quad (9)$$

where $m_{omNa-MMT}$ is the mass of the omNa-MMT nanoparticles (7 wt. %), m_{pm} is the mass of the polymer matrix material (93 wt. %), $D_{omNa-MMT}$ is the density of the omNa-MMT nanoparticles (2.66 g.cm^{-3}), and D_{pm} is the density of the polymer matrix material (1.17 g.cm^{-3}).

On substitution, the volume fraction of the omNa-MMt nanoparticles was determined to be 0.034. This value was then used to determine the interlayer spacing of the nanoparticles (X nm) in the EP matrix. From the calculation, it was determined that the incorporation of 7 wt. % omNa-MMt nanoparticles into the matrix of the EP matrix will expand the particles by 26.03 nm. This simply means that for an ideal packing, the d-spacing of the nanoparticles in the EP matrix will be about 26.03 nm making it possible to obtain an exfoliated nanostructure at 7 wt. % loading.

Before the synthesis of the EP-R-omNa-MMt nanocomposite coatings, epoxy resin was first modified with EHTPB in the proportion as given in *Table 5*. The DBTDL was first dissolved in DOS to prepare approximately 5 wt. % solution of D-12. About 1 wt. % D-12 of the total mass of the EHTPB and TDI was added to a three-neck flask containing ethyl acetate and stirred vigorously to obtain a uniform mixture. The EHTPB was thereafter added to the solution and allowed to completely dissolve. TDI was added to the solution in a dropwise manner while carrying out the pre-polymerization of the composite at 75°C for about 3 h. Afterwards, ethyl acetate of DGEBA epoxy resin was added to the flask and the mixture was held at 70°C – 80°C and stirred at 2500 rpm for another 2.5 h to obtain a pre-polymer solution. A constant amount of A60 was added to the pre-polymer solution after cooling to room temperature with vigorous stirring for

about 10 min. The EP-EHTPB solution was transferred into Teflon moulds and the solvent was removed at room temperature under a vacuum to obtain the EP-modified film (*Fig. 1)*

To synthesize the EP-R-omNa-MMt nanocomposite coatings, various amounts of modified Na-MMt in the proportion as given in *Table 5.* were dispersed in 50 ml ethyl acetate and stirred vigorously for about 1 h followed by bath sonication for an additional hour. The nanoclay suspension was then added to the prepolymer solution obtained at 70°C during the epoxy modification as described earlier. The mixed compositions containing the organoclay nanoparticles and resin were sonicated for about 150 min. During ultrasonication of the prepolymer solution, the sonication power was gradually increased while maintaining the mixture temperature at 50°C – 70°C by placing the reaction vessel in a cool water jacket. A constant amount of A60 was added to the prepolymer solution after cooling to room temperature with vigorous stirring for about 10 min. Subsequent curing procedure was followed as in the case of the modified epoxy resin (*Fig. 1).*By transferring the EP-R-omNa-MMt solution to the Teflon moulds, samples for further characterization were prepared. To prepare the pristine epoxy coating film, a certain amount of EP was added to the three-neck flask containing ethyl acetate and allowed to completely dissolve. A constant amount of A60 was then added to the EP solution with vigorous stirring for about 10 min. The curing procedure as earlier described was followed and the solution was transferred to Teflon moulds for mechanical and physicochemical test sample preparation.

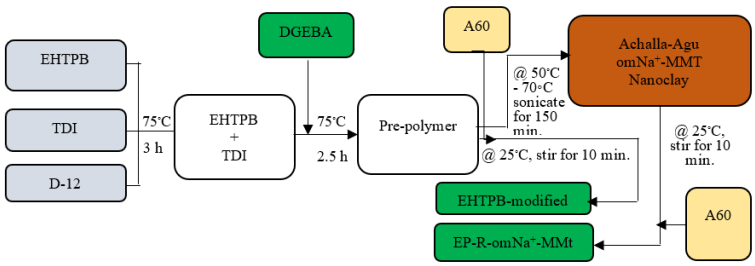


Fig. 1. Synthesis procedure for EHTPB-modified and EP-R-omNa-MMt coating film.

2.3.2 | Surface preparation and coating application

The 5L X52 HSLA pipe substrates were first preheated to eliminate moisture and enhance adhesion properties. Subsequently, the pipe materials were shot and grit blasted to achieve a clean surface with an appropriate anchor pattern profile before the application of coatings. The prepared steel sheet surface was coated with EP, EP-R, and EP-R-omNa-MMt using a micrometre film applicator with a wet film thickness of 50 µm. After coating, the samples were degassed in a desiccator to eliminate entrapped air bubbles and allowed to cure for 3 weeks under laboratory atmospheric conditions. The Dry-Coated Film Thickness (DFT), measured with a digital coating thickness meter, averaged around 30 ± 3 µm. Visual inspections of the coated films were conducted to identify blisters, foreign inclusions, and wrinkles.

2.3.3 | Characterization of polymer nanocomposite coatings

The reference coupons (EP and EP-R) and synthesized polymer nanocomposite coatings (EP-R-omNa-MMt) were prepared for structure/morphology, mechanical, adhesion, and permeability analyses. The bonding effects of EHTPB and A60 curing agent on the microstructure of the modified epoxy composite at the molecular level were evaluated using a FTIR spectrometer. This involved preparing samples from the scratched surface of the reference coupons, followed by mixing the samples with KBr and grinding to less than 5 mm. The mixture was further ground for 3 to 5 minutes for thorough blending. Subsequently, the sample-KBr powder was compressed to form an FTIR disk sample at 40 psi for about 2 minutes. The FTIR data were recorded in the wavelength range of 500 - 4000 cm^{-1} at 4 cm^{-1} resolution and a scan time of 64 sec. The changes in the structure of the modified EP at the molecular level were evaluated from the recorded FTIR spectra using a computerized recorder attached to the machine. The structure/morphology of the

synthesized nanocomposite anticorrosion coatings was determined by characterizing the degree of nanoparticle dispersion within the matrix of the EP using XRD and SEM techniques. For XRD analysis, samples, approximately 10 μm thick, were prepared and mounted on the XRD to record XRD patterns. The analysis utilized Cu-Kα radiation with a wavelength of 0.154 nm, at 40 kV operating voltage and 40 mA current, within a diffraction angle range of 2° to 10°, while for SEM analysis, Samples were mounted on SEM stubs using conductive carbon tubes and coated with gold using a sputtering technique for conductivity. The SEM analysis, conducted at an accelerating voltage of 8 kV with a beam current of 40 – 50 μA, provided detailed images of the samples from Secondary Electrons (SE). The effects of omNa-MMt nanoparticles and EHTPB on the tensile property and impact performance of the synthesized protective coatings were examined according to [21], [22] standards respectively. Tensile strength and elongation at break of reference coupons and synthesized nanocomposite protective coatings were determined using a universal tensile testing machine. Dumbbell tensile specimens conforming to [21] standards (*Fig. 2)* were machined, and measurements were obtained with a crosshead speed of 10 mm/min and a gauge length of 10 mm. Four specimens per coupon were prepared and analyzed, with the mean values recorded. For impact strength, the coatings were applied on large steel plates. These plates were subsequently sectioned into smaller pieces.

Fig. 8 illustrates the specimen after undergoing the cutting process, resulting in the desired dimensions of 100mm x 100mm. A V-shaped notch was created in the centre of the coated side of the panel and the panel was secured to the test apparatus using a suitable fixture. The pendulum, initially at its zero point, was recorded for the initial reading, then released from a predetermined height, impacting the coated panel at the notched area. Impact energy was determined based on pendulum mass and velocity. A thorough visual examination of the coated specimens was carried out to identify any damage, such as cracking, chipping, or coating detachment. The nature and extent of observed damage were documented. The fracture toughness of the EHTPB-modified epoxy composite was reaffirmed by sputtering fractured surfaces with a thin layer of gold. SEM analysis of the prepared samples, conducted at an accelerating voltage of 8 kV with a beam current of 40–50 μA, provided insight into the morphology of the fractured surfaces.

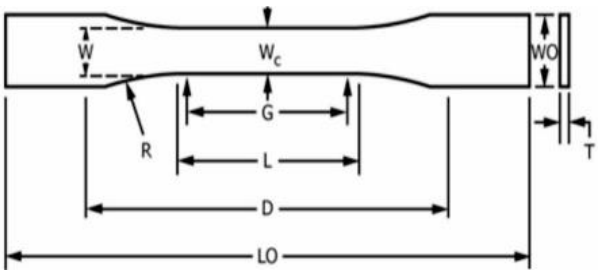


Fig. 2. ASTM dumbbell-shape tensile specimen.

Since the synthesized nanocomposite protective coating is intended for use in oilfield, the effects of organoclay nanoparticles and EHTPB on the adhesion and barrier properties were determined according to [23], [24] standards respectively. The adhesion test involves making six parallel cuts, 2 mm apart, on the blemish-free coated film using a tempered steel rule, each cut being 20 mm in length. The cut surface was brushed gently to remove detached flakes or ribbons. Additional perpendicular cuts were made, and the area was examined for light reflection from the substrate. A strip of tape was firmly rubbed onto the grid area using a pencil eraser, left for about 90 seconds, and then removed rapidly at an angle close to 180°. The grid area was inspected under magnification, and adhesion strength was rated according to the scale, as depicted in [23] *Fig. 3*.

For barrier properties analysis, approximately 3.5 g of material was pre-heated at 260 °C for 30 s and then compressed into thin films under 15 MPa pressure for 10 s using a 2.0 mm thick flat square thin film mould, allowing cooling at room temperature. Visual inspections ensured the absence of imperfections. The film thickness, measured to the nearest 0.0025 mm, was determined as 2.0 mm. Before mounting on the test dish, 2 mm thick square specimens underwent overnight soaking in water to achieve moisture equilibrium. Moisture absorption represented by weight gain exclusively from the desiccant was sealed in a semi-barrier over the test dish containing anhydrous calcium chloride desiccant. Paraffin wax and aluminium tape sealed the edges. The weight increase of the assembly was periodically monitored in a controlled chamber with a temperature (T) of 23°C and Relative Humidity (RH) of 75%.

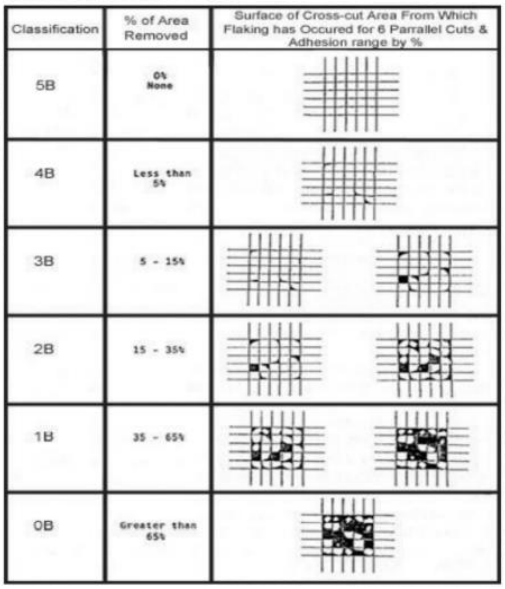


Fig. 3. ASTM D3359-02 scale for adhesion test.

2.3.4 | Corrosion behaviour of synthesized polymer nanocomposite coatings

About four types of samples were prepared and tested in both the gravimetric and electrochemical corrosion experiments: 1) blank (uncoated steel sheets), 2) coated with cured pristine EP, 3) coated with EHTPB-modified (EP-R), and 4) coated with Epoxy-R-omNa-MMt Nanocomposite coatings. The total exposure period for corrosion measurement in both the gravimetric and electrochemical experiments was 1,440 h (60 days).

2.3.5 | Gravimetric corrosion measurement

The laboratory accelerated corrosion immersion test was carried out at ambient temperatures in a typical 5000 mL resin flask having a reflux condenser with an atmospheric seal, a sparger for controlling atmosphere or aeration, a thermowell and temperature-regulating device, and a specimen support system as described in *Fig. 4* [25]. Before exposure, air-dried specimens were weighed on an analytical balance to an accuracy of at least ± 0.5 mg to determine their initial weight before mounting on the Teflon holders. A test solution with a composition (100% saturated + 3.5 wt. % NaCl) conforming to the Specifications of the Committee on Analytical Reagents of the American Chemical Society was accurately prepared for the experiment. The specimens were stamped with an appropriate identifying mark. Thereafter, the mounted samples were immersed in the prepared corrosive medium for a total exposure period of 1,440 h (60 days) to examine their anticorrosion behaviour. Specimens were mounted such that complete insulation from each other physically and electrically was achieved. Also, samples were insulated from any metallic container or supporting device used within the apparatus. Free contact of the samples with the corroding solution was ensured after mounting.

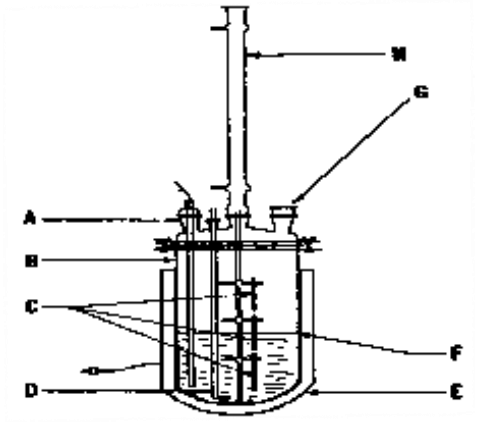


Fig. 4. Immersion corrosion test flask setup.

Legend:

A = thermowell.

B = resin flask.

C = specimens hung on supporting device.

D = air inlet.

E = heating mantle.

F = liquid interface.

G = opening in flask for additional apparatus that may be required.

H = reflux condenser.

Changes in the composition of the test solution were properly monitored and the evaporation losses during the experiment were controlled by frequent addition of an appropriate amount of the prepared corrosive solution to maintain the original volume within ± 1 % in the flask. At the end of every exposure period, samples were removed from the Teflon holders and thoroughly cleaned by scrubbing using a bristle brush and mild abrasive. The mechanically cleaned samples were thereafter washed with distilled water to remove all corrosion products from their surface.

The washed samples were dried overnight in a vacuum and reweighed with an accuracy corresponding to that of the original weighing. The weight loss during the periods of exposure for each sample was determined and recorded according to the standard [25]. The anticorrosion behaviour of each of the exposed coated samples was measured and recorded by determining the corrosion rates of the sample in the corrosive medium using the weight loss at the exposure periods.

2.3.6 | Electrochemical corrosion measurement

The standard test method was used to evaluate the electrochemical corrosion behaviour of the samples after exposure to the 3.5 % NaCl accelerated corrosion environment at test periods [26]. The rapid, nondestructive Electrochemical Impedance Spectroscopy (EIS) measurements were conducted using a conventional three-electrode corrosion glass cell which comprised Ag/AgCl as the reference electrode, graphite rod as the counter electrode, and coated samples as the working electrode.

The impedance measurements were carried out on samples with a total exposed surface area of 1 cm^2 in a 3.5 wt. % NaCl solution electrolyte at 25^oC. The samples for electrochemical corrosion measurement were scanned over a frequency range of 10,000 Hz (10 kHz) to 0.1 Hz (100 MHz) at a potential amplitude of 10

mV with respect to the OCP. Ten frequency points per decade were selected and the OCP for all samples and times of exposure were determined accordingly.

3 | Results and Discussion

3.1 | Epoxidized Hydroxyl-Terminated Polybutadiene -Modified Epoxy Polymer

The FTIR results in *Fig. 5* show band peak assignments for the pristine EP, EHTPB, and cured EP-EHTPB polymers. Epoxy groups have a characteristic absorption band at 913 cm^{-1}, which disappeared after curing, while the peak of the ester bonds was observed at 1733 cm^{-1} in the spectrum of the EP-EHTPB modified EP. This was due to the reaction between epoxy groups and amine-based curing agent, suggesting that the EHTPB-modified EP had been adequately cured.

The disappearance of a peak at 1640 cm^{-1} assigned to the vibration of C=C upon curing demonstrated the participation of the EHTPB double bond openings in the reaction process. The FTIR result is consistent with recent studies. For example, a study by [27] identified similar peaks in the FTIR spectra, including the strong absorption at 3340 cm^{-1} due to -OH stretching, and peaks at 2964 cm^{-1}, 2928 cm^{-1}, and 2870 cm^{-1} related to -CH stretching. The disappearance of the 913 cm^{-1} peak post-curing, indicating the reaction of epoxy groups, and the appearance of the 1733 cm^{-1} ester bond peak, corroborate the findings by [28], who also observed these changes indicating successful curing and the reaction of epoxy with amine-based curing agents.

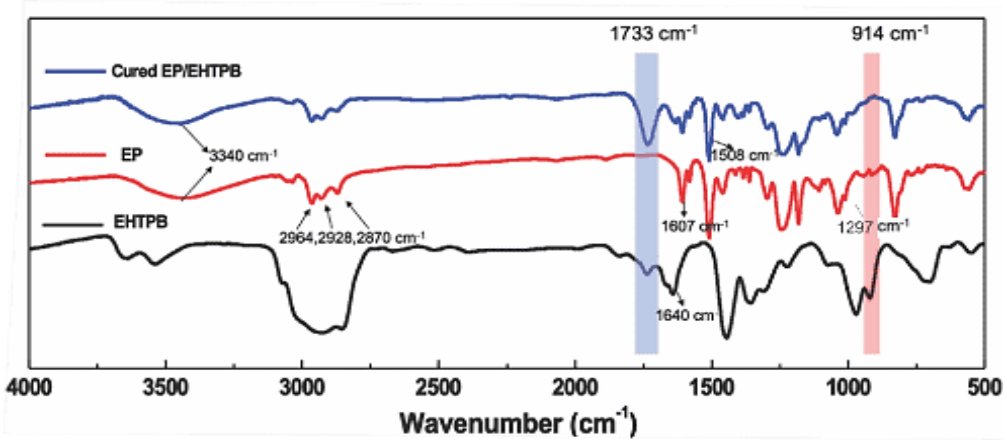


Fig. 5. Degree of EP-EHTPB epoxy polymer modification.

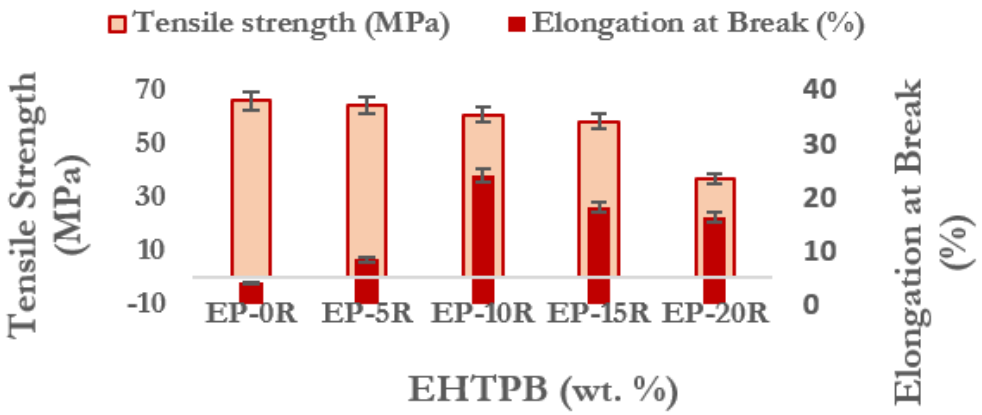


Fig. 6. Tensile properties of modified EP-EHTPB coatings

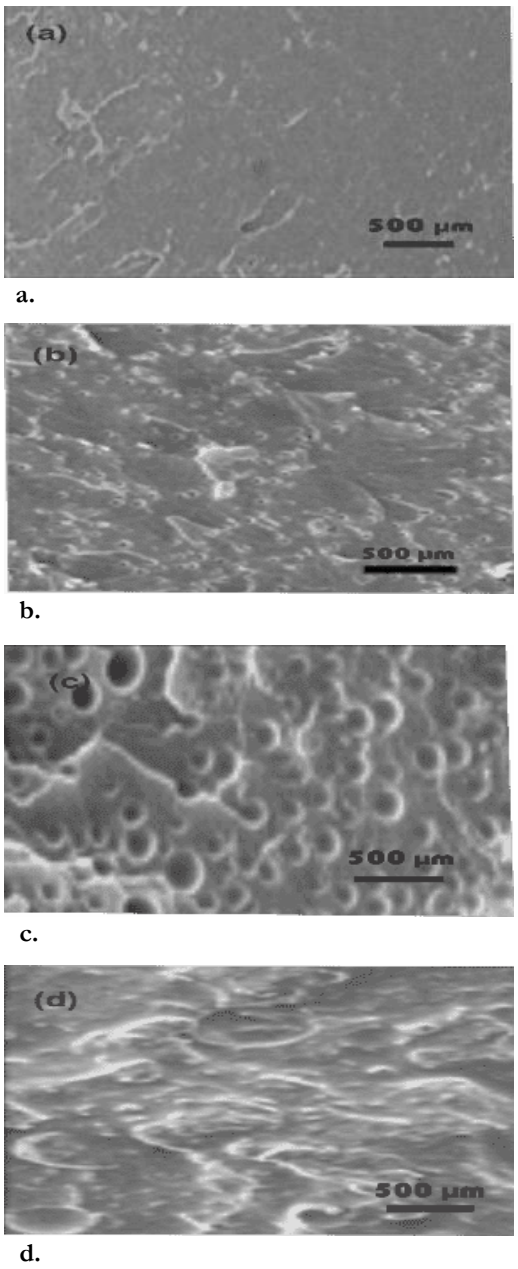


Fig. 7. Fracture surface toughness of modified EP-EHTPB epoxy polymer.

The findings in *Fig. 2* indicate a consistently high level of ductility and tensile strength performance of the EP-10R formulation, supporting the findings of other researchers who noted that well-cured epoxy formulations tend to exhibit low variability in mechanical properties [29]. The results demonstrates a compromise in the mechanical properties of the EHTPB-modified EP composite. For example, higher elongation at break and lower tensile strength were observed for the EHTPB-modified EP. Besides, compared to the cured pristine EP resin, the elongation at break for 10 wt. % EHTPB-modified EP increased by over 500 %, while its tensile strength was reduced by about 7.63 %. This agrees with the results from [30], who observed that the incorporation of elastomers in epoxy resins significantly improves ductility and toughness but reduces tensile strength. A marginal decrease in tensile strength at no more than 10 wt. % EHTPB was observed for the EHTPB-modified EP indicating a significant improvement in ductility and toughness. Specifically, optimum mechanical strengths of the EHTPB-modified EP were achieved at 10 wt. % EHTPB loading. This result is similar to the improvements reported by [31], who found that the additions of elastomers enhance toughness without severely compromising tensile strength.

In addition, the micrographs in *Fig. 7* show the toughening effect of EHTPB on the EHTPB-modified polymer composites. The surface morphology of the fractured pristine EP as depicted in *Fig. 7.a* shows a

smooth and glassy surface without any filaments, which indicates the behaviour of brittle polymers undergoing a brittle failure. Meanwhile, tortuous and surface roughness were observed with increased EHTPB content indicating high toughness or ductile property. The SEM micrograph of the 5 wt. % EHTPB in *Fig. 7.b* showed a greater number of striations and folding when compared with the morphological characteristics of the pristine EP. As was observed in *Fig. 7.c*, the microstructural roughness and tortuous surface were much higher in the 10 wt. % EHTPB, suggesting the highest toughness and ductility. The transition from a smooth, glassy surface in pristine EP, which indicates a brittle failure, to a rough, tortuous surface in 10 wt. % EHTPB-modified composites agree with the findings of [32], who noted similar morphological changes correlating with enhanced toughness. The observed plastic cavitation and increased cross-linking density, which slow fracture growth rates and enhance toughness, are consistent with the toughening mechanisms described by [33]. These mechanisms involve the formation of carbamate and oxazolidinone structures, resulting in more branched chains and a denser cross-linked network, which improves mechanical properties.

3.2|EP-R-omNa-MMt Nanocomposite Coatings

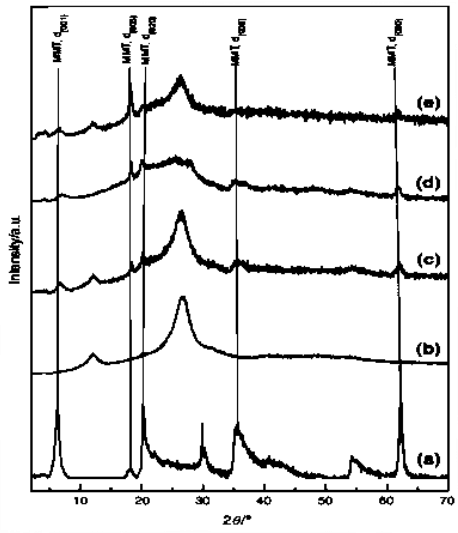
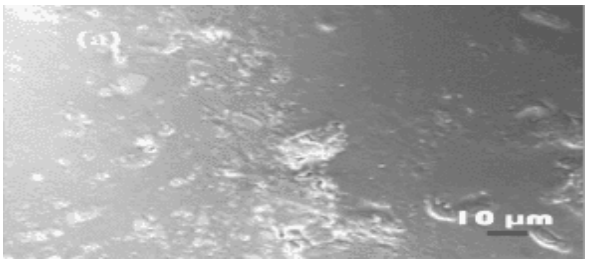
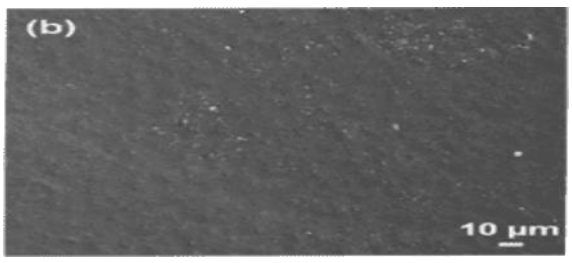


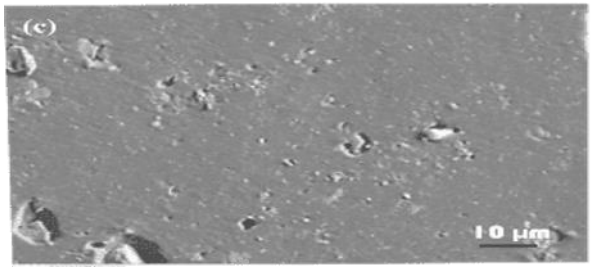
Fig. 8. XRD pattern of nanocomposite coatings; a. omNa-MMt, b. EP-10R-1omNa-MMt; c. EP-10R-3omNa-MMt, d. EP-10R-5omNa-MMt, and e. EP-10R-7omNa-MMt.



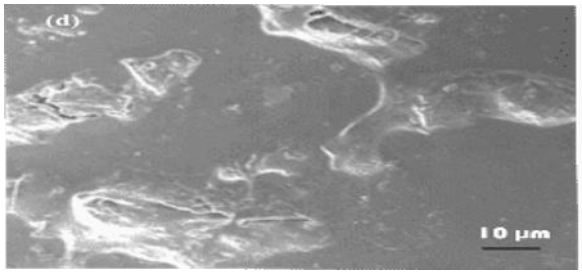
a.



b.



c.



d.

Fig. 9. Morphologies of nanocomposite coatings; a. EP-10R-1omNa-MMt; b. EP-10R-3omNa-MMt; c. EP-10R-5omNa-MMt, and d. EP-10R-7omNa-MMt.

The XRD diffractograms in *Fig. 9* demonstrate the degree of nanoparticle dispersion (structure) within the matrix of the synthesized polymer nanocomposite coatings by comparing them with that of the omNa-MMt. From the results, the characteristic peak for omNa-MMt *Fig. 9.a* appeared at about 2.44° 2θ which relates to a d-spacing of 3.62 nm calculated using the Brag equation. The main peak in the X-ray diffraction patterns of the omNa-MMt was due to the formation of interlayer spaces by regular stacking of the silicate layers. In addition, the XRD pattern of the EP-10R-1omNa-MMt nanocomposite coating was observed to be similar to that of an amorphous DGEBA polymer *Fig. 9.b*. This was due to the small amount of omNa-MMt nanoparticles, < 3 wt. %, in the matrix of the polymer, causing no diffraction during the analysis. However, with the dispersion of about 3 wt. % omNa-MMt into the matrix of the EHTPB-modified EP *Fig. 9.c*, the characteristic diffraction peak at 2.44° 2θ disappeared suggesting a complete exfoliated nanocomposite structure. Moreover, with an increased clay content of about 5 wt. % omNa-MMt (*Fig. 9.d*), a small and broad new peak appeared at a lower angle (2.04° 2θ) than that of the omNa-MMt, indicating an intercalated structure with bigger space between the clay platelets. This new peak became broader with high omMMt content *Fig. 9.d*. It was observed that at high omMMt contents, complete exfoliation was hindered resulting in an increased degree of intercalations. Recent studies by [34–36] have also observed similar behavior. They noted that at lower concentrations, nanoparticles are well-dispersed and tend to exfoliate, leading to improved mechanical properties. However, at higher concentrations, particles tend to agglomerate, forming intercalated structures that might not provide the same level of property enhancement due to poor dispersion and increased viscosity of the matrix.

The SEM micrographs presented in *Fig. 9* further confirmed the morphology of the polymer nanocomposite coatings. The morphology of EP-10R-1wt. % omNa-MMt coating as represented in *Fig. 9.a* is similar to that observed for the unmodified EP with only small agglomerates of nanoparticles, suggesting an intercalated structure. However, more dispersed nanofillers into the organic matrix were observed for EP-10R-3wt % omNa-MMt coating *Fig. 9.b*. The morphology of the EP-10R-3wt. % omNa-MMt shows a well-separated nanoclay layers which are dispersed quasi-homogenously in the continuous matrix of the polymer, suggesting a complete exfoliated nanocomposite structure. This agrees with the XRD results. On the other hand, a small ratio of intercalated structure was observed for EP-10R-5wt. % omNa-MMt, indicating poor bonding between the partially dispersed omMMt nanofillers and the polymer matrix *Fig. 9.c*. At higher omMMt contents, intercalated nanoclay aggregates with irregular-shape morphology were observed for EP-10R-7wt. % omNa-MMt coating *Fig. 9.d*, suggesting an intercalated nanostructure. From *Fig. 9*, the formation of an

exfoliated nanocomposite coating was achieved with up to 3 wt. % omMMt, whereas intercalated structures were observed for nanocomposite coatings with 1, 5, and 7 wt. % omMMt contents.

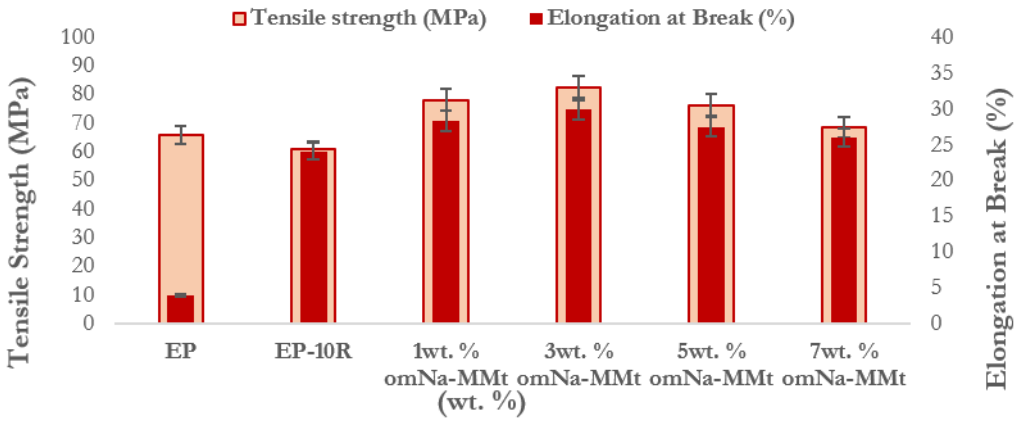


Fig. 10. Tensile properties of epoxy-rubber-omNa-MMt nanocomposite coating.

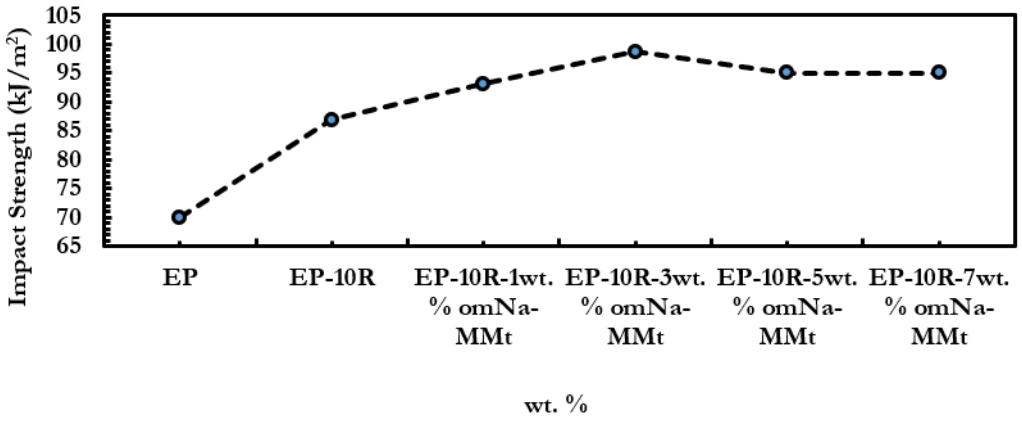


Fig. 11. Impact behaviour of epoxy-rubber-omNa-MMt nanocomposite coating.

The nanocomposite coatings demonstrated higher stress values compared to the unmodified and modified epoxy, suggesting enhancements in tensile strength with the addition of EHTPB rubber and organoclay nanoparticles (*Fig. 10.*) The addition of rubber (EP-10R) slightly reduced the tensile strength compared to the EP. However, a substantial increase in elongation at break was observed, indicating improved flexibility and ductility with the introduction of rubber.

Increasing the weight % of organoclay nanoparticles from 0 to 7 in EP-10R coating formulations showed an improvement in tensile strength. The highest tensile strength was observed in EP-10R-3wt. % omNa-MMt, suggesting an optimum concentration (*Fig. 10.*) EP-10R-3wt. % omNa-MMt has the highest UTS (81.5789 MPa), suggesting an improved tensile strength compared to formulations with 1wt. %, 5wt. %, and 7wt. % omNa-MMt. The elongation at break shows a decreasing trend with higher organoclay content, indicating a potential trade-off between strength and flexibility.

The optimum balance between strength and flexibility was achieved in EP-10R-3wt. % omNa-MMt, as it demonstrated relatively high tensile strength along with optimal elongation at break. Its elongation at break was observed to be about 30%, indicating considerable ductility. This property is important in applications where materials are subjected to deformation before failure.

Table 6. Adhesion strength of EP and synthesized nanocomposite coatings.

Sample	Test Tape Result	Rating	Description
EP-0R-0omNa-MMt	No visible coating removal.	5B	Excellent adhesion; no evidence of coating detachment.
EP-10R-0omNa-MMt	No blistering or loss of adhesion.	5B	Excellent adhesion and resistance to detachment.
EP-10R-1wt. % omNa-MMt	Blistering less than 5% of the crosshatched area.	4B	The majority of the coating remains firmly attached.
EP-10R-3wt. % omNa-MMt	Absence of blistering or detachment of the coating.	5B	The coating exhibits excellent adhesion and resistance to detachment.
EP-10R-5wt. % omNa-MMt	Less than 5% crosshatched area blistering.	4B	The greater part of the coating stays securely adhered.
EP-10R-7wt. % omNa-MMt	Blistering affects less than 5% of the crosshatched area.	4B	The majority of the coating adheres securely to the substrate.

As shown in *Fig. 11*, the impact strength result reveals that the pristine coating (EP), without the incorporation of rubber and organoclay, exhibited an impact energy of 2.8 J and a strength of 70 kJ/m², leading to total failure (*Table 6.) Fig. 11* shows that the introduction of 10 wt.% rubber resulted in an improvement in impact strength (3.475 J, 86.875 kJ/m²) with adhesion failure observed in the EP-10R formulation (*Table 6*.) The incorporation of 1 wt.% organoclay nanoparticles further enhances the impact strength of the EP-10R-1wt.% omNa-MMt (3.725 J, 93.125 kJ/m²) which experienced coating cracking during impact analysis.

A further increase in organoclay content to approximately 3 wt.% resulted in an optimal impact strength of 3.95 J (98.75 kJ/m²) with substrate failure observed (*Table 6.)* Subsequent increases in organoclay content as observed in EP-10R-5wt.% omNa-MMt and EP-10R-7wt.% omNa-MMt formulations resulted in a slight reduction in impact strength (3.8 J, 95 kJ/m²) with indentation failure. Based on the results, EP-10R-3wt.% omNa-MMt appears to have the highest impact strength and a substrate failure mode, which might indicate better performance under impact loading.

The increased impact strength can be attributed to the chemical interaction involving the reaction among the epoxide groups in DGEBA and those in EHTPB and additional hydrogen bond formation among the hydroxyl groups in EHTPB and other functional groups in the epoxy resin. This is in agreement with findings by [36], [37] which highlighted the importance of rubber in improving the adhesion at the interfacial plane and ductility of polymer composites.

This outcome can also be attributed to the synergistic effects of MMt clay reinforcement and rubber toughening, maintaining a balance between stiffness and toughness in the epoxy matrix. The rubber component effectively absorbs the impact energy, while the MMt reinforces the matrix, reducing the possibility of crack propagation. Additionally, the MMt particles acted as energy-dissipating entities, absorbing impact energy during the deformation process. This supports the findings of [38–41] highlighting the crucial balance needed between rubber and organoclay for optimal impact resistance in polymer composites. Higher nanoclay content beyond the optimal point leads to reduced impact strength due to increased brittleness and poor dispersion, which creates weak points in the composite structure [42], [43].

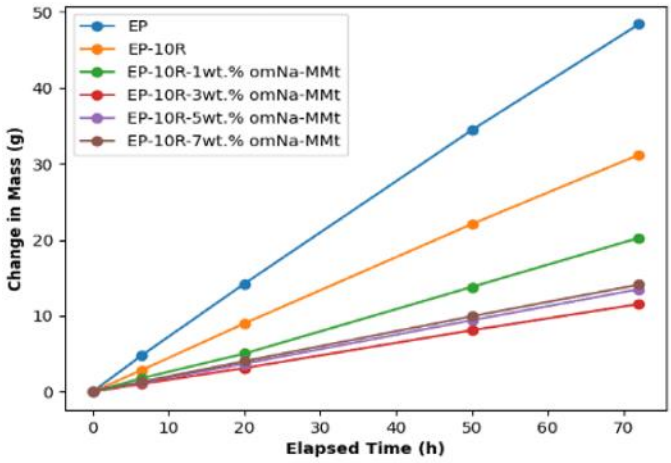


Fig. 12. Moisture uptake characteristics of EP coating formulations.

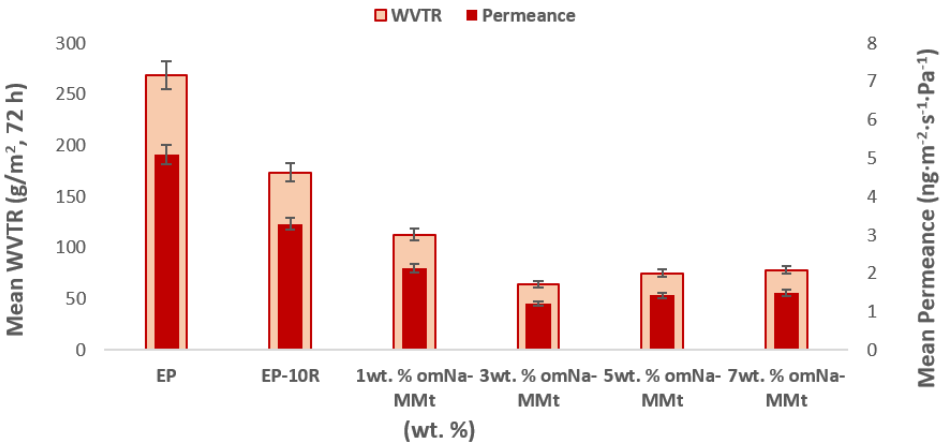


Fig. 13. Barrier properties of EP coating formulations.

The EP coating demonstrated a steady increase in weight as the elapsed time increased, reaching approximately 48.40 g at 72 hours (*Fig. 12*). Similarly, the EP-10R formulations, with varying concentrations of omNa-MMt, exhibited varying degrees of weight gain over time, reflecting their respective moisture absorption characteristics. The EP-10R-1wt.% omNa-MMt showed a comparatively lower weight gain, indicating reduced moisture absorption by the desiccant. This corresponds to the potential barrier properties attributed to the incorporation of omNa-MMt, as observed in similar studies on nanocomposite coatings [44],[45]. The EP-10R-3wt.% omNa-MMt, EP-10R-5wt.% omNa-MMt, and EP-10R-7wt.% omNa-MMt consistently show a progressive reduction in weight gain, suggesting an enhanced resistance to moisture absorption with higher concentrations of omNa-MMt.

The WVTR and WVP under a RH gradient of 52.7 % for EP coatings containing 10 wt. % EHTPB and various levels of organoclay are depicted in (*Fig. 13).* In the absence of EHTPB, a high WVTR and WVP of approximately 268.89 g/m².h and 5.102 ng·m^{-2}·s^{-1}·Pa^{-1} were observed for the EP (blank), indicating its inherent permeability. The introduction of 10 wt. % EHTPB in the EP-10R sample led to a gradual reduction in both WVTR and WVP compared to the EP coating (*Fig. 13).*

The observed decrease in WVTR and WVP of the modified EP-10R formulation may be attributed to alterations in the epoxy composition, impacting its moisture transport properties. Significantly, the introduction of 10 wt. % EHTPB into the EP coating film, in the absence of organoclay, resulted in a notable decrease in both WVTR and WVP, nearly twice the values. Specifically, WVTR decreased from 268.89 g/m²·h for the EP film to 173.56 g/m²·h for the EP-10R coating film, while WVP dropped from 5.102 ng·m^{-2}·s^{-1}·Pa^{-1} to 3.293 ng·m^{-2}·s^{-1}·Pa^{-1}. This reduction is attributed to the combined hydrophobic characteristics of EP and

EHTPB, acting synergistically to impede water transport. The influence of EHTPB on film barrier properties was more evident in the presence of organoclay. With the addition of 3 wt. % omNa-MMt nanoclay, both WVTR and WVP demonstrated a substantial decrease of approximately 76.19%, compared to the WVTR and WVP values observed in EP-10R coating formulation with 1 wt. % organoclay, which showed a decrease of about 58.04 %. Generally, the addition of hydrophobic compounds into a polymer matrix results in a reduced moisture uptake. Moisture content plays a role in film plasticity, with water acting as a plasticizer, thus influencing an increase in WVP.

However, with increased omNa-MMt of about 5 wt. % and 7 wt. % respectively, the formulations demonstrated a slightly higher mean WVTR and WVP compared to the EP-10R-3wt.% omNa-MMt (*Fig. 13*). The observed increase in mean WVTR and WVP is attributed to the higher concentrations of omNa-MMt which resulted in agglomeration and intercalated structure. Moreover, the aspect ratio of omNa-MMt, while contributing to improved barrier properties at lower concentrations, might reach a saturation point at higher concentrations. Beyond a certain amount, the increased concentration may not proportionally enhance the barrier performance of the nanocomposite coating. Additionally, the interplay of components and their interactions within the nanocomposite coating could become more complex at elevated concentrations, influencing the overall moisture permeability characteristics.

3.3 | Corrosion Behaviour of Synthesized Polymer Nanocomposite Coatings

Analyzing the weight loss and corrosion rates reveals a clear trend in the protective efficiency of the coatings. The results (*Figs. 14-16)* illustrated that the X52 base (uncoated) metal experienced a consistent increase in weight loss and corrosion rate over the period of exposure. After seven days of exposure, these values were approximately 16 mg and 1.03 mm/yr respectively. Subsequently, after sixty days, both the weight loss and corrosion rate increased to about 184 mg and 1.43 mm/yr, indicating higher susceptibility of the steel to corrosion attack. However, the EP and EP-0R coatings showed improved performance, reducing the weight loss to about 10 mg and 8 mg by the seventh day, and 21 mg and 19 mg by the sixtieth day, respectively, in comparison to the uncoated X52 steel substrate. A decrease in corrosion rates, measuring between 0.68 mm/yr and 0.54 mm/yr, was noted for the EP and EP-0R coatings following 168 hours of exposure *Fig. 15*.

This resulted in corrosion protection efficiencies of about 34% and 48%, respectively (*Fig. 16)*. The protection efficiency saw an additional improvement, reaching approximately 89 % and 90 % for the EP and EP-0R coatings after a cumulative exposure period of 1440 hours *Fig. 16*.

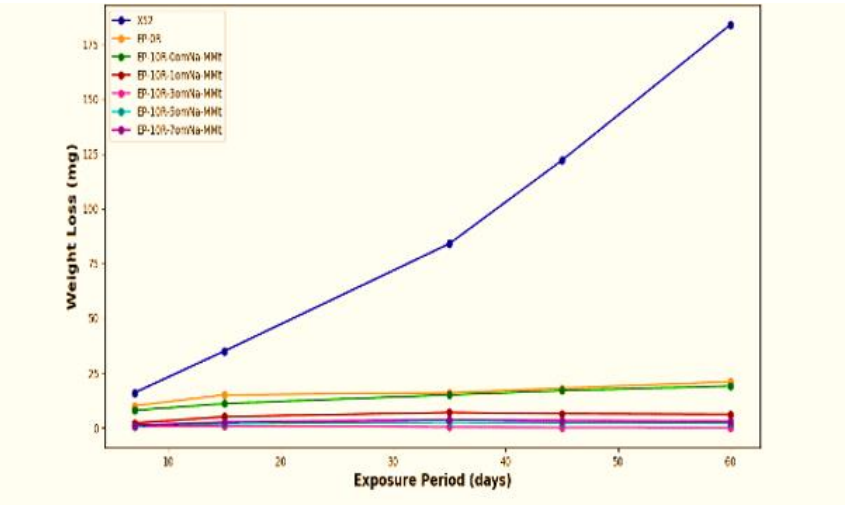


Fig. 14. Weight loss for corrosion immersion tests of various coatings.

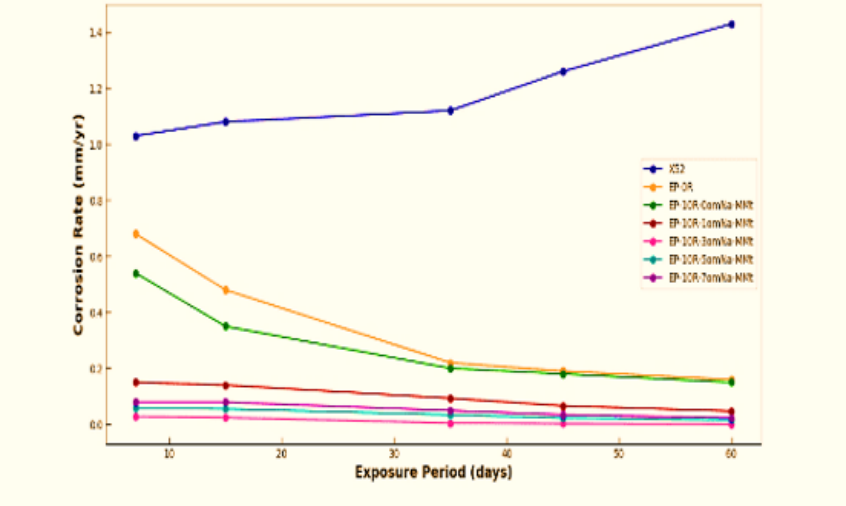


Fig. 15. Corrosion rates of EP coating formulations.

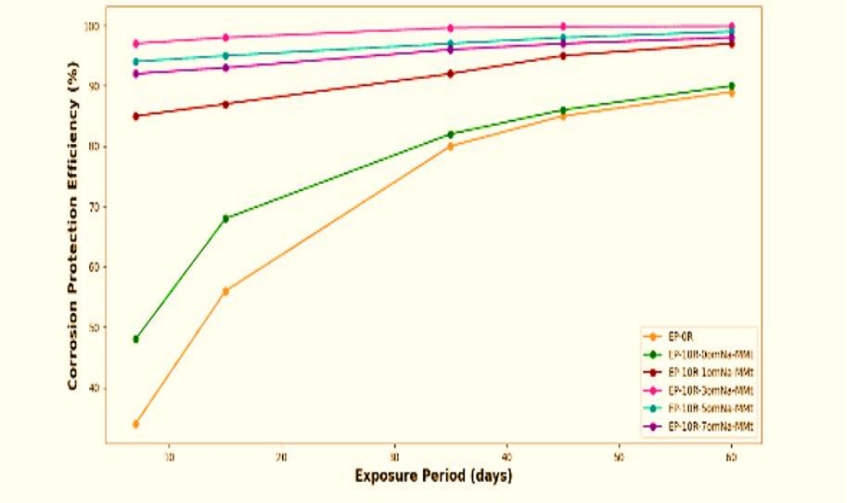


Fig. 16. Corrosion protection efficiency of EP coating formulations.

However, as organoclay nanoparticles were introduced in the EP-10R formulations, a substantial per cent decrease in weight loss and corrosion rates was observed, with EP-10R-3wt.% omNa-MMt demonstrating the most significant improvement *Figs. 14-16*. At about 168 hours of exposure, the nanocomposite coatings exhibited significant enhancement in protection, with minimal weight loss values of about 2.2 - 0.4 mg, and corrosion rates of 0.15 – 0.028 mm/yr. These values represent approximately 86 % to 98 % reduction after seven days of exposure compared to the uncoated X52 steel specimen and a 76 % to 96 % reduction compared to the pristine EP. This trend continued with prolonged exposure to approximately 360, 840, and 1080 hours, where EP-10R-3wt.% omNa-MMt consistently showed a higher percentage decrease in both weight loss and corrosion rate compared to the uncoated X52 steel substrate. With an increased immersion period of 1440 hours, the EP-10R-1omNa-MMt, EP-10R-5omNa-MMt, and EP-10R-7omNa-MMt demonstrated reduced weight losses of about 6 mg, 2 mg, and 3 mg, along with corrosion rates of 0.047 mm/yr, 0.015 mm/yr, and 0.023 mm/yr, respectively. These results represent protection efficiencies of 97%, 99%, and 98%, respectively, when compared to the uncoated X52 steel substrate *Fig. 16*. Although EP-10R-5omNa-MMt showed greater protection efficiency when compared to the pristine EP and EP-10R formulations, its weight loss and corrosion rate were higher than those of the EP-10R-3omNa-MMt nanocomposite coating after 1440 hours of immersion period. The corrosion rate of EP-10R-3omNa-MMt was found to be remarkably lower at 0.0008 mm/yr, and its corrosion protection efficiency consistently increased to approximately 99.9 % after 60 days of exposure (*Fig. 16).*

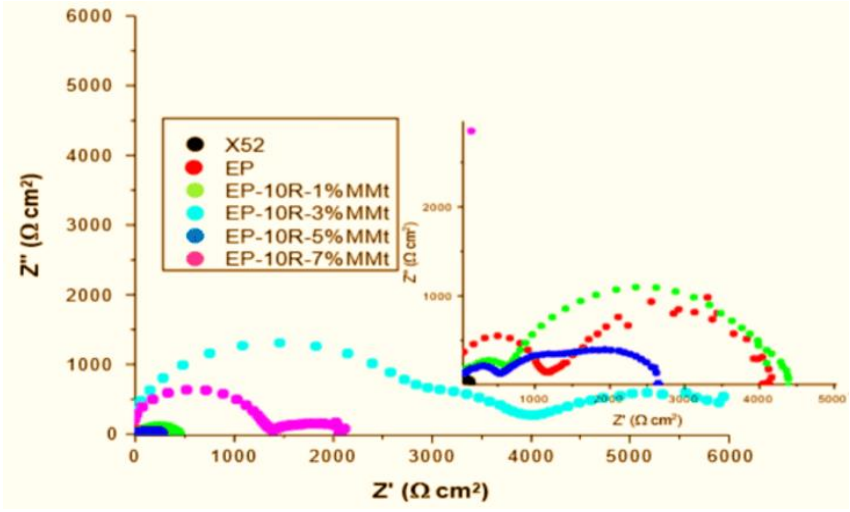


Fig. 17. Nyquist curves for bare X52, EP, and EP-10R-omMMt nanocomposites coated X52 substrates after seven (7) days immersion.

Table 7. EIS Corrosion parameters after seven (7) days of exposure.

Sample	R_s (Ω cm²)	$R_{ct.}$ (Ω cm²)	Cdl (μF cm^{-2})	C_f (μF cm^{-2})	R_p (Ω cm²)	PE (%)
X52 (uncoated)	5.8	4.3	210	134	210	-
EP	44	27	350	0.25	330	36
EP-10R-1wt. % omNa-MMt	52	14	199	0.15	1620	87
EP-10R-3wt. % omNa-MMt	84	35	33	1.6	11400	98
EP-10R-5wt. % omNa-MMt	42	8	129	2.1	5380	96
EP-10R-7wt. % omNa-MMt	45	6.7	133	2.3	5250	96

EIS studies were performed to observe the low frequencies of the coatings after the first 7 days and 60 days of immersion which are shown in *Figs. 17* and *18* in order to further investigate the corrosion protection efficiency. Increased impedance at lower frequencies signifies a more efficient coating. The semi-circled shape observed in the Nyquist plot (*Fig. 17)* indicates that the EP-10R nanocomposite coating formulations exhibited both capacitive and resistive properties after 168 hours of exposure period. The Nyquist curves showed increased semicircle diameter with higher omMMt content, indicating an increasing charge-transfer resistance up to an optimal level, beyond which it decreases again. However, this trend peaks at an optimal omMMt content of 3 % before declining. The Nyquist plots support the result of the corrosion rates, indicating that the 3% omMMt loading exhibited the highest impedance at the low-frequency region. However, a decrease in corrosion protection efficiency at 7 % omMMt loading was observed. To quantitatively compare the corrosion protection efficiencies of the different coatings, the EIS data were fitted in an equivalent circuit, and the resulting electrochemical parameters as detailed in *Table 7*. were obtained. The polarization resistance (Rp) value of the pristine EP-coated steels was lower than those of the EP-10R formulations. Furthermore, these values demonstrated enhancement in the formulated coatings where omMMt nanoparticles were incorporated. This again reveals that the addition of omNa-MMt enhances the corrosion resistance of the coating better than the pristine EP. The synthesized coatings incorporated with nanofillers had PE values above 87 %, which is a significant increase compared to samples coated with pristine EP coatings. These findings illustrate that incorporating nanoparticles as fillers can significantly improve the corrosion resistance of polymer coatings. The observed trend in these values is consistent with the results obtained from the weight loss measurements. This indicates that after a seven-day exposure period, the EP-10R-3omNa-MMt exhibited the highest Rp value of 98%.

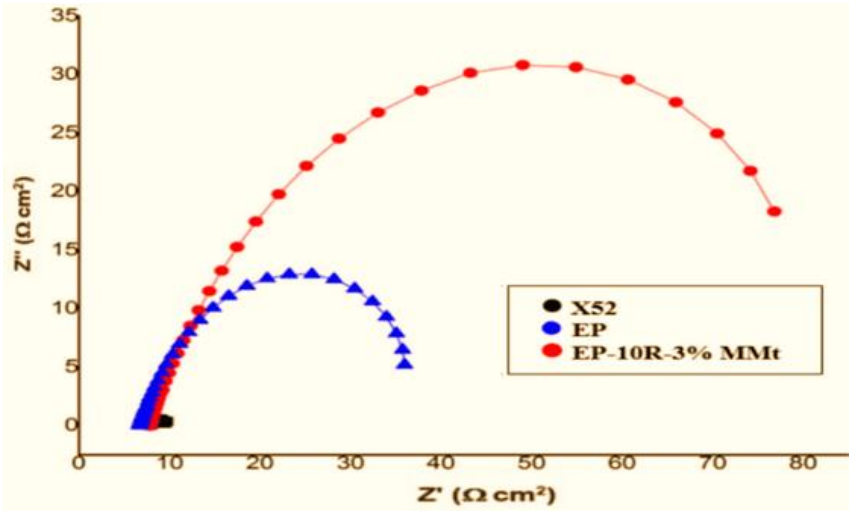


Fig. 18. Nyquist curves of bare X52 steel, and EP, EP-10R-3% MMt coated X52 substrates immersed in 3.5 wt. % NaCl for sixty (60) days.

Table 8. Resistance values (Ω cm²) of samples after sixty (60) days of exposure.

Parameters of Equivalent Circuit	X52 (Uncoated)	EP	EP-10R-3wt. % omNa-MMt
R_s	9.24	16.8	78.2
R_1	3.72	6.55×10^{2}	5.43×10^{4}
Y_{01}	3.97×10^{-2}	4.47×10^{-2}	9.99×10^{-6}
n_1	5.21×10^{-1}	7.24×10^{-1}	1.00
R_2	1.04×10^{2}	4.38×10^{2}	2.22×10^{5}
Y_{02}	8.98×10^{-2}	4.22×10^{-2}	9.83×10^{-6}
n_2	8.67×10^{-1}	3.43×10^{-1}	7.11×10^{-1}
R_{tot} ($R_1 + R_2$)	1.08×10^{2}	10.93×10^{2}	2.76×10^{5}

For comparison, the Nyquist plots also supported the results obtained from the weight loss measurements after sixty (60) days of exposure to the chloride-rich corrosion environment. Examination of the bare and coated X52 substrates in *Fig. 18* reveals that both the pristine EP and EP-10R-3omNa-MMt coatings resulted in a substantial reduction in the corrosion rate of the HSLA steel. The pristine EP coating reduced the corrosion rate to approximately 89 % compared to that of the bare X52 steel, whereas the EP-10R-3omNa-MMt coating resulted in a significant decrease in corrosion rate, amounting to about 99.9 % than that of the bare X52 substrate. The EP-10R-3omNa-MMt coating demonstrated higher stability, resulting in a corrosion rate of more than eleven times lower than that of the pristine EP. The EIS measurements conducted after a sixty-day exposure period, as presented in *Table 8*. showed an increased total resistance (R_{tot}) for the pristine EP coating (R_p). Meanwhile, the EP-10R-3omNa-MMt coating exhibited higher R_{tot} values than the pristine EP, suggesting an enhanced corrosion protection efficiency. The R_{tot} value increased from 1.08×10^2 (Ω cm²) for the bare X52 steel to 10.93×10^2 (Ω cm²) for pristine EP, and further to 2.76×10^5 (Ω cm²) for the EP-10R-3omNa-MMt coated X52 substrate after 1440 hours of exposure *(Table 8.)* The lower R_{tot} value of the bare X52 steel supports the findings from the weight loss measurements, which demonstrated a consistent increase in weight loss of the steel over the period of exposure, suggesting a constant corrosion rate. The increase in R_{tot} value observed for the pristine EP-coated X52 steel indicates an improved corrosion protection efficiency of the coating after 1440 hours of exposure. However, the determined R_{tot} value for the pristine EP coating was significantly smaller than that of the EP-10R-3omNa-MMt nanocomposite coating, indicating a higher corrosion rate in comparison. The EP-10R-3omNa-MMt coated X52 steel exhibited the highest R_{tot} value, showing further enhancement in the corrosion protection efficiency of the synthesized nanocomposite coating.

Comparing these results with recent findings reveals notable similarities and differences. For instance, studies by [46], [47] reported that incorporating nanoparticles in polymer coatings significantly enhances corrosion

resistance, which agrees with the current findings that the EP-10R-3wt.% omNa-MMt coatings provide substantial protection. Pourhashem et al. [46] observed that low nanoparticle loadings enhanced dispersion and exfoliation, resulting in better protective properties. This supports the enhanced corrosion protection efficiency of the EP-10R-3wt.% omNa-MMt coating observed in this study. Further comparisons show that the protection resistance of EP and EP-10R coatings improved over the exposure period, with EP-10R-3wt.% omNa-MMt achieving the highest protection efficiency of 99.9% after 60 days of exposure. This observation is consistent with studies by [48–50], which reported the long-term corrosion protection efficiency of epoxy coatings at optimal nanoparticle content. Furthermore, the poor corrosion protection performance at higher nanoparticle loadings due to aggregation, as noted with EP-10R-5wt.% omNa-MMt and EP-10R-7wt.% omNa-MMt, is consistent with findings by [41], [51].

4 | Conclusion

In conclusion, the study on polymer-rubber-organoclay nanocomposite coatings offers a promising strategy for enhancing corrosion protection in subsea pipeline applications. The study addresses the crucial need for nanocomposite coatings that can effectively withstand the continuous corrosion challenges present in marine corrosion environments. The synthesis of polymer nanocomposite coatings, incorporating indigenous organoclay MMt nanoparticles and polybutadiene rubber as reinforcing agents, resulted in coatings with improved mechanical, barrier, and adhesion properties compared to those of the pristine EP. FTIR analysis shows a transformation reaction between the epoxy groups and the amine-based curing agent at an absorption band of 913 cm^{-1} and ester bond of 1733 cm^{-1}, demonstrating the successful curing of EP-EHTPB-modified epoxy. EHTPB increases the elongation at break while reducing tensile strength. At 10 wt. % EHTPB loading, the optimum balance of mechanical properties was achieved, demonstrating enhanced ductility and toughness. The SEM micrographs show a transition from brittle to ductile behaviour with higher EHTPB content. Plastic cavitation in the 10 wt. % EHTPB formulation signifies reduced fracture growth, demonstrating strong interaction between EHTPB and epoxy for improved toughness and mechanical properties. However, above 15 wt. % EHTPB leads to rubber phase aggregation, resulting in a reduction of the desired properties. From the XRD diffractograms and SEM micrographs, an exfoliated nanocomposite coating was achieved with up to 3 wt. % omMMt, while intercalated structures were observed for 1, 5, and 7 wt. % omMMt contents. The EP-10R coating formulation with 3 wt. % omMMt had better mechanical, barrier, and adhesion properties than those formulated with 1, 5, and 7 wt. % omMMt. This is due to better dispersion/exfoliation of the nanolayers in the EP matrix as supported by SEM, XRD, tensile, impact, and adhesion tests. Results of the chemical/electrochemical corrosion measurements showed that the pristine EP, EP-10R and EP-10R nanocomposite coating formulations exhibited better anti-corrosion properties. The pristine EP and EP-10R coatings provided substantial protection to the X52 steel substrate from corrosion in the chloride-rich environment. This is attributed to the low water absorption capability of EP which inhibited the corrosive species from reaching the X52 steel substrate through the coating surface. The incorporation of omMMt nanoparticles further enhanced the corrosion protection efficiency of the nanocomposite coatings with an optimum loading of 3 wt. % organoclay MMt. Further increase led to the agglomeration of nanofillers which affected the protection efficiency of the coatings as evidenced by the chemical/electrochemical corrosion measurements. The enhanced mechanical, barrier, and adhesion properties of the EP-10R-3wt.% omNa-MMt nanocomposite coating, coupled with its high protection efficiency in the chloride-rich environment, make it more suitable for subsea corrosion applications.

Declaration of Competing Interest

The authors declare that they have no competing financial interests or personal relationships that could have appeared to influence the work reported in this paper.

Acknowledgments

My profound gratitude goes to every staff member of the Mechanical and Aerospace Engineering Department, University of Uyo, who in one way or another has contributed to the success of this study. I also wish to acknowledge the motivation and contribution I got from Engr. Prof. A. Offiong.

Authors' Contributions

All research activities and manuscript development were conducted by the author, who also approved the final manuscript.

Data Availability

All data are included in the text.

Funding

This research was not supported by any specific grant from funding bodies in the public, commercial, or not-for-profit sectors.

Conflict of Interest

There are no competing interests to declare.

Consent for Publication

The authors consent to the publication of this manuscript.

Ethics Approval and Consent to Participate

The authors confirm that this research did not involve human participants or animal subjects.

References

[1] Mokhatab, S., Poe, W. A., & Mak, J. Y. (2012). Raw gas transmission. *Handbook of Natural Gas Transmission and Processing, 2nd Ed.; Gulf Professional Publishing: Waltham, Ma, Usa*, 103–176. https://doi.org/10.1016/C2010-0-66115-3

[2] Menon, E. S. (2014). *Transmission pipeline calculations and simulations manual*. Gulf Professional Publishing. https://doi.org/10.1016/C2009-0-60912-0

[3] Rehman, K., & Nawaz, F. (2017, March). Remote pipeline monitoring using wireless sensor networks. In *2017 International conference on communication, computing and digital systems (C-CODE)* (pp. 32-37). IEEE. https://doi.org/10.1109/C-CODE.2017.7918897

[4] Xiao, Q., Li, J., Sun, J., Feng, H., & Jin, S. (2018). Natural-gas pipeline leak location using variational mode decomposition analysis and cross-time–frequency spectrum. *Measurement*, *124*, 163-172. https://doi.org/10.1016/j.measurement.2018.04.030

[5] Arifin, B. M. S., Li, Z., Shah, S. L., Meyer, G. A., & Colin, A. (2018). A novel data-driven leak detection and localization algorithm using the Kantorovich distance. *Computers & Chemical Engineering*, *108*, 300-313. https://doi.org/10.1016/j.compchemeng.2017.09.022

[6] Jia, Z., Wang, Z., Sun, W., & Li, Z. (2019). Pipeline leakage localization based on distributed FBG hoop strain measurements and support vector machine. *Optik*, *176*, 1–13. https://doi.org/10.1016/j.ijleo.2018.09.048

[7] Nazir, M. H., Saeed, A., & Khan, Z. (2017). A comprehensive predictive corrosion model incorporating varying environmental gas pollutants applied to wider steel applications. *Materials Chemistry and Physics*, *193*, 19-34. https://doi.org/10.1016/j.matchemphys.2017.01.081

[8] Bolotina, I., Borikov, V., Ivanova, V., Mertins, K., & Uchaikin, S. (2018). Application of phased antenna arrays for pipeline leak detection. *Journal of Petroleum Science and Engineering*, *161*, 497–505. https://doi.org/10.1016/j.petrol.2017.10.059

[9] Al-Janabi, Y. T. (2020). An overview of corrosion in oil and gas industry: Upstream, midstream, and downstream sectors. *Corrosion Inhibitors in the Oil And Gas Industry*, 1-39. https://doi.org/10.1002/9783527822140.ch1

[10] Tamalmani, K., & Husin, H. (2020). Review on corrosion inhibitors for oil and gas corrosion issues. *Applied Sciences*, *10*(10), 3389. https://doi.org/10.3390/app10103389

[11] Merachtsaki, D., Xidas, P., Giannakoudakis, P., Triantafyllidis, K., & Spathis, P. (2017). Corrosion protection of steel by epoxy-organoclay nanocomposite coatings. *Coatings*, *7*(7), 84. https://doi.org/10.3390/coatings7070084

[12] Bergaya, F., & Lagaly, G. (2013). *Handbook of clay science* (Vol. 5). Newnes. https://doi.org/10.1016/C2011-1-06768-1

[13] Su, L., Fang, C., & Luo, H. (2024). Functionalized montmorillonite/epoxy resin nanocomposites with enhanced thermal and mechanical properties. *RSC Advances, 14*, 31251–31258. https://doi.org/10.1039/D4RA03125C

[14] Asgari, M., Abouelmagd, A., & Sundararaj, U. (2017). Silane functionalization of sodium montmorillonite nanoclay and its effect on rheological and mechanical properties of HDPE/clay nanocomposites. *Applied Clay Science*, *146*, 439–448. https://doi.org/10.1016/j.clay.2017.06.035

[15] Niroumand, J. S., Peighambardoust, S. J., & Shenavar, A. (2016). Polystyrene-based composites and nanocomposites with reduced brominated-flame retardant. *Iranian Polymer Journal*, *25*(7), 607–614. https://doi.org/10.1007/s13726-016-0451-7

[16] Bahreini, Z., Heydari, V., & Namdari, Z. (2017). Effects of nano-layered silicates on mechanical and chemical properties of acrylic-melamine automotive clear coat. *Pigment & Resin Technology*, *46*(5), 333-341. https://doi.org/10.1108/PRT-07-2016-0077

[17] Agwu, O. E., Okon, A. N., & Udoh, F. D. (2015, August). A review of Nigerian bentonitic clays as drilling mud. In *SPE Nigeria annual international conference and exhibition* (pp. SPE-178264). SPE. https://doi.org/10.2118/178264-MS

[18] Ombaka, O. (2016). Characterization and classification of clay minerals for potential applications in Rugi Ward, Kenya. *African Journal of Environmental Science and Technology*, *10*(11), 415-431. https://doi.org/10.5897/AJEST2016.2184

[19] Afolabi, R. O., Orodu, O. D., & Efeovbokhan, V. E. (2017). Properties and application of Nigerian bentonite clay deposits for drilling mud formulation: Recent advances and future prospects. *Applied Clay Science*, *143*, 39-49. https://doi.org/10.1016/j.clay.2017.03.009

[20] Morgan, A. B., & Gilman, J. W. (2003). Characterization of polymer-layered silicate (clay) nanocomposites by transmission electron microscopy and X-ray diffraction: A comparative study. *Journal of Applied Polymer Science*, *87*(8), 1329-1338. https://doi.org/10.1002/app.11884

[21] ASTM International. (2022). *Standard test method for tensile properties of plastics (ASTM D638-22)*. ASTM International. https://doi.org/10.1520/D0638-22

[22] ASTM International. (2010). S*tandard test method for resistance of organic coatings to the effects of rapid deformation (impact) (ASTM D2794-93(2010))*. ASTM International. https://doi.org/10.1520/D2794-93R10

[23] ASTM International. (2002). *Standard test methods for measuring adhesion by tape test (ASTM D3359-02)*. ASTM International. https://doi.org/10.1520/D3359-02

[24] ASTM International. (2016). *Standard test methods for water vapor transmission of materials (ASTM E96/E96M-16)*. ASTM International. https://doi.org/10.1520/E0096_E0096M-16

[25] ASTM International. (2004). *Standard practice for laboratory immersion corrosion testing of metals (ASTM G31-72(2004))*. ASTM International. https://doi.org/10.1520/G0031-72R04

[26] ASTM International. (2003). *Standard test method for measurement of impedance of anodic coatings on aluminum (ASTM B457-67(2003))*. ASTM International. https://doi.org/10.1520/B0457-67R03

[27] Mahantesha, B. K., Ravindrachary, V., Padmakumari, R., Sahanakumari, R., Tegginamata, P., Sanjeev, G., & Verma, V. P. (2019). Effect of electron irradiation on optical, thermal and electrical properties of

polymer electrolyte. *Journal of Radioanalytical and Nuclear Chemistry*, *322*(1), 19–27. https://doi.org/10.1007/s10967-019-06462-4

[28] Silva, A. A. C., Gomes, T. I., Martins, B. D. P., Garcia, R. B. R., Cividanes, L. D. S., & Kawachi, E. Y. (2020). New insights in adhesive properties of hybrid epoxy-silane coatings for aluminum substrates: effect of composition and preparation methods. *Journal of Inorganic and Organometallic Polymers and Materials*, *30*(8), 3105–3115. https://doi.org/10.1007/s10904-020-01468-y

[29] Rudawska, A. (2021). Mechanical properties of selected epoxy adhesive and adhesive joints of steel sheets. *Applied Mechanics*, *2*(1), 108-126. https://doi.org/10.3390/applmech2010007

[30] Białkowska, A., Bakar, M., Kucharczyk, W., & Zarzyka, I. (2023). Hybrid epoxy nanocomposites: Improvement in mechanical properties and toughening mechanisms—A review. *Polymers*, *15*(6), 1398. https://doi.org/10.3390/polym15061398

[31] Dai, P., Luo, X., Yang, Y., Kou, Z., Huang, B., Zang, J., & Ru, J. (2020). High temperature tensile properties, fracture behaviors and nanoscale precipitate variation of an Al--Zn--Mg--Cu alloy. *Progress in Natural Science: Materials International*, *30*(1), 63–73. https://doi.org/10.1016/j.pnsc.2020.01.007

[32] Fugolin, A. P. P., Costa, A. R., Correr Sobrinho, L., Crystal Chaw, R., Lewis, S., Ferracane, J. L., & Pfeifer, C. S. (2021). Toughening and polymerization stress control in composites using thiourethane-treated fillers. *Scientific Reports*, *11*(1), 7638. https://doi.org/10.1038/s41598-021-87151-9

[33] Zotti, A., Zuppolini, S., Zarrelli, M., & Borriello, A. (2016). Fracture toughening mechanisms in epoxy adhesives. In *Adhesives-Applications and Properties*. IntechOpen. https://library.oapen.org/bitstream/handle/20.500.12657/115134/9789535127840.pdf?sequence=1#page=249

[34] Khan, I., Saeed, K., & Khan, I. (2019). Nanoparticles: Properties, applications and toxicities. *Arabian Journal of Chemistry*, *12*(7), 908–931. https://doi.org/10.1016/j.arabjc.2017.05.011

[35] Archibong, F. N., Orakwe, L. C., Ogah, O. A., Mbam, S. O., Ajah, S. A., Okechukwu, M. E., & Ikelle, I. I. (2023). Emerging progress in montmorillonite rubber/polymer nanocomposites: A review. *Journal of Materials Science*, *58*(6), 2396-2429.

[36] Archibong, F. N., Orakwe, L. C., Ogah, O. A., Mbam, S. O., Ajah, S. A., Okechukwu, M. E., & Ikelle, I. I. (2023). Emerging progress in montmorillonite rubber/polymer nanocomposites: A review. *Journal of Materials Science*, *58*(6), 2396-2429. https://doi.org/10.1007/s10853-023-08173-4

[37] Cazan, C., Cosnita, M., & Duta, A. (2017). Effect of PET functionalization in composites of rubber–PET–HDPE type. *Arabian Journal of Chemistry*, *10*(3), 300-312. https://doi.org/10.1016/j.arabjc.2015.10.005

[38] Liang, Y. L., & Pearson, R. A. (2010). The toughening mechanism in hybrid epoxy-silica-rubber nanocomposites (HESRNs). *Polymer*, *51*(21), 4880-4890. https://doi.org/10.1016/j.polymer.2010.08.052

[39] Bakar, M., & Szymańska, J. (2014). Property enhancement of epoxy resin using a combination of amine-terminated butadiene–acrylonitrile copolymer and nanoclay. *Journal of Thermoplastic Composite Materials*, *27*(9), 1239-1255. https://doi.org/10.1177/0892705712470265

[40] Razavi Nouri, M., & Karami, M. (2014). Effect of rubber content on morphology and thermal and rheological behaviors of acrylonitrile-butadiene rubber/poly (ethylene-co-vinyl acetate)/organoclay nanocomposites. *Polymer*, *55*(26), 6940-6947. https://doi.org/10.1016/j.polymer.2014.10.050

[41] Dadrasi, A., Gharebagh, A. A., & Fooladpanjeh, S. (2016). Optimization of mechanical properties of rubber/silica/epoxy nanocomposites by RSM. *International Journal*, *2347*, 6710. https://doi.org/10.15680/IJIRSET.2015.0506281

[42] Levy, P. S., & Lemeshow, S. (2013). *Sampling of populations: Methods and applications (4th Ed.)*. John Wiley & Sons. https://doi.org/10.1002/9780470374597

[43] Montgomery, D. C., & Runger, G. C. (2019). *Applied statistics and probability for engineers*. John wiley & sons. https://www.wiley-vch.de/en/

[44] Nguyen Tri, P., Nguyen, T. A., Carriere, P., & Ngo Xuan, C. (2018). Nanocomposite coatings: Preparation, characterization, properties, and applications. *International Journal of Corrosion*, *2018*(1), 4749501. https://doi.org/10.1155/2018/4749501

[45] Schiessl, S., Kucukpinar, E., Cros, S., Miesbauer, O., Langowski, H. C., & Eisner, P. (2022). Nanocomposite coatings based on polyvinyl alcohol and montmorillonite for high-barrier food packaging. *Frontiers in Nutrition*, *9*, 790157. https://doi.org/10.3389/fnut.2022.790157

[46] Pourhashem, S., Saba, F., Duan, J., Rashidi, A., Guan, F., Nezhad, E. G., & Hou, B. (2020). Polymer/Inorganic nanocomposite coatings with superior corrosion protection performance: A review. *Journal of Industrial and Engineering Chemistry*, *88*, 29–57. https://doi.org/10.1016/j.jiec.2020.04.029

[47] Samad, U. A., Alam, M. A., Abdo, H. S., Anis, A., & Al Zahrani, S. M. (2023). Synergistic effect of nanoparticles: enhanced mechanical and corrosion protection properties of epoxy coatings incorporated with SiO2 and ZrO2. *Polymers*, *15*(14), 3100. https://doi.org/10.3390/polym15143100

[48] Maksimović, M. D., & Mišković-Stanković, V. B. (1992). The corrosion behaviour of epoxy-resin electrocoated steel. *Corrosion Science*, *33*(2), 271–279. https://doi.org/10.1016/0010-938X(92)90151-R

[49] Radhamani, A. V, Lau, H. C., & Ramakrishna, S. (2020). Nanocomposite coatings on steel for enhancing the corrosion resistance: A review. *Journal of Composite Materials*, *54*(5), 681–701. https://doi.org/10.1177/0021998319857807

[50] Nazari, M. H., Zhang, Y., Mahmoodi, A., Xu, G., Yu, J., Wu, J., & Shi, X. (2022). Nanocomposite organic coatings for corrosion protection of metals: A review of recent advances. *Progress in Organic Coatings*, *162*, 106573. https://doi.org/10.1016/j.porgcoat.2021.106573

[51] Chai, C., Yin, F., Li, G., & Luo, Y. (2015). Mechanical and thermal properties of mesogen-jacketed liquid crystalline polymer/epoxy resin composites. *Science China Chemistry*, *58*(6), 1021–1026. https://doi.org/10.1007/s11426-015-5372-3